

# Hydrogen-Induced Conversion of SnS<sub>2</sub> into SnS or Sn: A Route to Create SnS<sub>2</sub>/SnS Heterostructures

James Felton,\* Elena Blundo, Zakhar Kudrynskiy, Sanliang Ling, Jonathan Bradford, Giorgio Pettinari, Timothy Cooper, Matthew Wadge, Zakhar Kovalyuk, Antonio Polimeni, Peter Beton, David Grant, Gavin Walker, and Amalia Patanè\*

The family of van der Waals (vdW) materials is large and diverse with applications ranging from electronics and optoelectronics to catalysis and chemical storage. However, despite intensive research, there remains significant knowledge-gaps pertaining to their properties and interactions. One such gap is the interaction between these materials and hydrogen, a potentially vital future energy vector and ubiquitous processing gas in the semiconductor industry. This work reports on the interaction of hydrogen with the vdW semiconductor SnS<sub>2</sub>, where molecular hydrogen (H<sub>2</sub>) and H-ions induce a controlled chemical conversion into semiconducting-SnS or to β-Sn. This hydrogen-driven reaction is facilitated by the different oxidation states of Sn and is successfully applied to form SnS<sub>2</sub>/SnS heterostructures with uniform layers, atomically flat interfaces and well-aligned crystallographic axes. This approach is scalable and offers a route for engineering materials at the nanoscale for semiconductor technologies based on the earth-abundant elements Sn and S, a promising result for a wide range of potential applications.

## 1. Introduction

2D materials based on van der Waals (vdW) crystals possess unique physical and chemical properties, providing an exciting platform for scientific research and technological developments. These properties, including a large surface area to volume ratio, high tensile strength, and novel electronic band structures that do not have counterparts in traditional systems, have been widely researched.<sup>[1–4]</sup> Yet, many of the fundamental properties and interactions of these systems, outside the headline materials of graphene, transition metal dichalcogenides, and MXenes,<sup>[5–7]</sup> remain poorly understood. One important interaction is that with hydrogen, a common processing gas in the semiconductor industry and touted future energy vector.

To date, studies of the interactions of both molecular and charged hydrogen species with vdW crystals have revealed a rich diversity of interesting phenomena. Physisorption, chemisorption, and intercalation of molecular hydrogen have all been demonstrated in graphene under different conditions.<sup>[8–10]</sup> The diffusion mechanisms of hydrogen through a graphene or hBN sheet have also attracted significant interest.<sup>[11,12]</sup> Also, hydrogen can bind to the lattice of a 2d semiconductor, such as InSe or form hydrogen filled interlayer surface bubbles in MoS<sub>2</sub>.<sup>[13,14]</sup> In general, whether a bond is formed between hydrogen and another atom depends on numerous factors, such as its electronegativity, co-ordination, and oxidation state. The ability to predict different phenomenologies based on these factors remains elusive and is pivotal to potential future applications in fields ranging from electrocatalysis, hydrogen sensing, hydrogen storage, and hydrogen purification to device fabrication and defect engineering.<sup>[15–18]</sup> This is very valuable when considering the challenges that these fields all face and the important role hydrogen plays in traditional semiconductors.<sup>[19,20]</sup>

Amongst 2D materials, vdW crystals based on Sn and S offer an interesting platform for hydrogen studies. They can exist in a variety of stoichiometries, lattice structures, and with Sn atoms in the different oxidation states Sn<sup>4+</sup>, Sn<sup>2+</sup>, and Sn<sup>0</sup>.<sup>[21]</sup> For the Sn(IV) state in SnS<sub>2</sub>, a vdW crystal is formed with an hexagonal crystal structure and P3m1 symmetry (**Figure 1a**). For the Sn(II) state, found in SnS, a vdW crystal is formed


J. Felton, Z. Kudrynskiy, J. Bradford, P. Beton, A. Patanè  
School of Physics and Astronomy  
University of Nottingham  
Nottingham NG7 2RD, UK  
E-mail: james.felton1@nottingham.ac.uk;  
amalia.patane@nottingham.ac.uk

E. Blundo, A. Polimeni  
Dipartimento di Fisica  
Sapienza Università di Roma  
Roma 00185, Italy

S. Ling, T. Cooper, M. Wadge, D. Grant, G. Walker  
Advanced Materials Research Group  
Faculty of Engineering  
University of Nottingham  
Nottingham NG7 2RD, UK

G. Pettinari  
Institute for Photonics and Nanotechnologies (CNR-IFN)  
National Research Council  
Rome 00156, Italy

Z. Kovalyuk  
Institute for Problems of Materials Science  
National Academy of Sciences of Ukraine  
Chernivtsi Branch, Chernivtsi 58001, Ukraine

 The ORCID identification number(s) for the author(s) of this article can be found under <https://doi.org/10.1002/sml.202202661>.

© 2022 The Authors. Small published by Wiley-VCH GmbH. This is an open access article under the terms of the Creative Commons Attribution License, which permits use, distribution and reproduction in any medium, provided the original work is properly cited.

DOI: 10.1002/sml.202202661

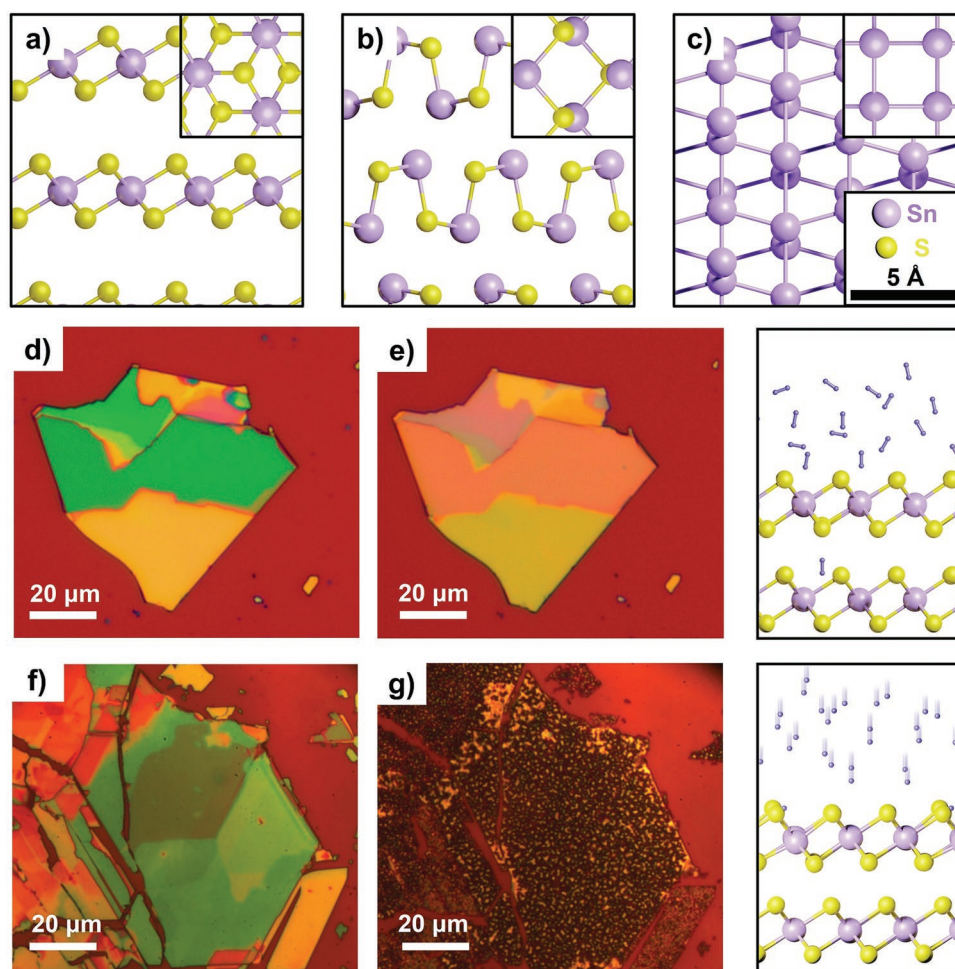
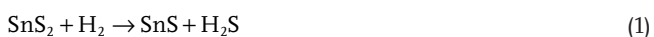


**Figure 1.** Side-view (main) and in-plane view (inset) of the crystals structure of a)  $\text{SnS}_2$ , b)  $\text{SnS}$ , and c)  $\beta\text{-Sn}$ . The scale bar (0.5 nm) is the same for all panels. These crystal structures were generated using previously gathered data.<sup>[27,28]</sup> Optical microscopy images of  $\text{SnS}_2$  on an Au/Si substrate d) before exposure to  $\text{H}_2$ , e) after exposure to  $\text{H}_2$ , f) before exposure to H-ions, and g) after exposure to H-ions. (right panels) Sketches of the exposure of  $\text{SnS}_2$  to  $\text{H}_2$  and H-ions responsible for the transformation shown in parts (d,e) and (f,g), respectively.

with an orthorhombic PNMA phase (Figure 1b). Finally,  $\beta\text{-Sn}$  is found in elemental form as a covalent crystal in the  $\text{Sn}^0$  oxidation state (Figure 1c). Of particular interest are  $\text{SnS}_2$  and  $\text{SnS}$  as they are not only found as stable vdW crystals down to single layers, but their electronic and optical properties can be tuned by the layer thickness.<sup>[22,23]</sup> These materials have been incorporated as active components in water-splitting devices for the generation of hydrogen.<sup>[24–26]</sup> Furthermore, the ability of hydrogen to form bonds with sulfur, such as those found in  $\text{H}_2\text{S}$ , makes hydrogen a perfect candidate to modify these materials. As such, the interactions between hydrogen and  $\text{SnS}_2$  and  $\text{SnS}$  should be investigated.

In this work, we report on the deceptively simple reaction shown in Equation 1



with implications ranging from the chemical conversion of  $\text{SnS}_2$  into  $\text{SnS}$  to the formation of  $\text{SnS}_2/\text{SnS}$  heterostructures with atomically flat interfaces and tunable electronic, vibrational and optical properties. The interaction of  $\text{SnS}_2$  with H-ions leads instead to the conversion of  $\text{SnS}_2$  to  $\beta\text{-Sn}$ . Density

Functional Theory (DFT) is used to provide a theoretical basis for the experimental results and fundamental understanding of the interaction of hydrogen in Sn-S compounds. These findings offer a route for engineering physical properties at the nanoscale for semiconductor technologies based on earth-abundant elements, such as Sn and S, and facilitate their use across a wide range of emerging technologies.

## 2. Results

### 2.1. $\text{SnS}_2$ Thin Films Exposed to $\text{H}_2$ and H-Ions

$\text{SnS}_2$  flakes were exfoliated from bulk crystals grown by chemical vapor transport and then dry transferred onto either Au/Si or  $\text{SiO}_2/\text{Si}$  substrates.<sup>[29]</sup> These samples were then exposed to continually refreshed  $\text{H}_2$  gas (for details, see Experimental Section) with control over the pressure (within the range from  $5 \times 10^{-4}$  to  $7 \times 10^{-3}$  mbar) and temperature (over the range from 150 to 300 °C). Total exposure time varied from 3.5 to 8 h. Alongside the  $\text{H}_2$  exposed samples, a number of samples were

exposed to H<sup>+</sup> ions generated by a Kaufman ion source.<sup>[30]</sup> A final set of samples were annealed in vacuum at 150 °C for use as control samples.

The exposure of SnS<sub>2</sub> flakes to either H<sub>2</sub> or H<sup>+</sup> ions induces a visible change in their color and contrast. Figure 1d,e illustrates this transformation for a flake exposed to H<sub>2</sub> at  $7 \times 10^{-4}$  mbar at 150 °C for 75 h. It can be seen that the shape of the flake remains unchanged by the exposure, but the flake undergoes a color shift. In this instance, the originally green (center of flake Figure 1d) region is transformed into a light-orange tone (central Figure 1e), whilst an originally light red region takes on a yellow-orange color. The exact nature of the shift is dependent on the original, interference-induced, color of the flake. Similar effects were observed on several samples exposed at temperatures of up to 250 °C. However, at temperatures of 250 °C a strong etching of SnS<sub>2</sub> is observed alongside the appearance of dark-spots on the flake surface. When the exposure temperature is increased to 300 °C, the flakes are entirely etched away (Figure S1, Supporting Information).

Flakes of SnS<sub>2</sub> exposed to H<sup>+</sup> ions from a Kaufman ion source behave in a different way to those exposed to H<sub>2</sub>. Figure 1f,g show SnS<sub>2</sub> flakes before and after exposure to H<sup>+</sup> ions with a beam energy of 12 eV and a total dose of  $6 \times 10^{16}$  ions cm<sup>-2</sup> over 3.5 h at 150 °C. A typical response is shown with discoloration of the exposed flakes alongside the formation of black micron-sized plateau features (confirmed by the scanning electron microscopy (SEM) images shown in Figure S2, Supporting Information), leading to a disordered and rough surface. Also, the thinner flakes undergo a significant etching, which occurs over a wide range of temperatures, hydrogen doses and for flakes on both Au/Si and SiO<sub>2</sub>/Si substrates.

We mapped out the real-space distribution of different elements near the surface of representative samples by energy dispersive X-ray (EDX) spectroscopy coupled with SEM. These studies indicate an overall decrease of the S to Sn atomic ratio following the hydrogen treatment. This change becomes more pronounced in the samples exposed to H<sup>+</sup> ions where we observed a non-homogeneous etching of the surface. This is accompanied by the appearance of micrometer-size plateaus with a dominant Sn-content (Figure S2, Supporting Information) and inter-plateau regions with a composition similar to that of the pristine samples.

## 2.2. Chemical Conversion of SnS<sub>2</sub> by H<sub>2</sub> and H<sup>+</sup> Ions

We probed the chemical state of the atoms in the control and hydrogenated SnS<sub>2</sub> samples by X-ray photoelectron spectroscopy (XPS). The chemical environment of an atom can have a pronounced effect on the binding energies of core-level electrons, leading to a chemical shift that can be used to assess the effects of different surface treatments on the oxidation state of the atoms. Here, we focus on high resolution spectra gained for the Sn 3d core-level.

Figure 2 shows the XPS spectra in the Sn 3d regions of the control SnS<sub>2</sub>, H<sub>2</sub>-exposed SnS<sub>2</sub>, and H<sup>+</sup>-ions-exposed SnS<sub>2</sub> samples. The spectra were fitted using two or three Voigt functions to resolve the contribution from different oxidation states resulting from the chemical modification of SnS<sub>2</sub> by hydrogen

(Figure S3, Supporting Information). For the control sample, the Sn 3d doublet is clearly visible: two well-resolved single lines can be seen at binding energies of 486.9 and 495.3 eV. The principle peak at 486.9 eV is in agreement with the value of 486.7 eV for Sn<sup>4+</sup> reported for SnS<sub>2</sub> in the literature,<sup>[31]</sup> as is the 8.4 eV splitting.<sup>[32]</sup> For the H<sub>2</sub> exposed sample, the position of the Sn<sup>4+</sup> doublet remains visible and unchanged. However, additional features appear on the low energy side of both components of the doublet. Specifically, these features appear at 1.0 and 1.2 eV below the Sn<sup>4+</sup> low-energy and high-energy component, respectively (see green arrows in Figure 2a). The new features observed in the hydrogenated samples correlate with previous data for the Sn<sup>2+</sup> peak in SnS where the Sn 3d component has a binding energy of between 0.9 and 1.3 eV less than for the Sn<sup>4+</sup> peak in SnS<sub>2</sub>.<sup>[33–35]</sup>

For the SnS<sub>2</sub> exposed to H<sup>+</sup> ions, the XPS spectra reveal more significant changes: the Sn<sup>4+</sup> low-energy peak shifts to 486.6 eV, 0.3 eV lower than in the control sample, whilst the peak splitting remains at the expected 8.4 eV.<sup>[35]</sup> Two additional components can also be seen at 485.5 eV and at 484.8, 1.1, and 1.8 eV lower than the Sn<sup>4+</sup> peak, respectively (see purple arrows in Figure 2b). We assign these features to different oxidation states of Sn: Sn<sup>2+</sup> in SnS and the neutral states of Sn, in line with previously reported data for the Sn<sup>0</sup> peak in β-Sn (485.0 eV) and a Sn<sup>4+</sup>–Sn<sup>0</sup> separation of 2.0 eV.<sup>[33,35]</sup> We have examined samples exposed to different hydrogen treatments and all reveal similar XPS spectra, suggestive of a partial chemical conversion of SnS<sub>2</sub> onto SnS and/or β-Sn. No measurable trace of contamination due to the formation of a tin oxide could be resolved.

## 2.3. Formation of SnS<sub>2</sub>/SnS Heterostructures by H<sub>2</sub>

We have conducted a detailed investigation of the SnS<sub>2</sub> films exposed to H<sub>2</sub> using transmission electron microscopy (TEM) and atomic force microscopy (AFM). Here, we focus on the cross-sectional TEM images. As shown in Figure 3a), these reveal the formation of a SnS<sub>2</sub>/SnS heterostructure with a well-defined interface between the SnS and SnS<sub>2</sub> layers and a SnS layer of thickness of ≈10 nm. Figure 3b shows a more detailed view of the interface region: the individual vdW layers can be clearly seen and they are continuous. The characteristic paired-up rows of Sn atoms are visible in the SnS region of Figure 3c in line with the offset Sn atoms in individual vdW layers of SnS shown in Figure 1b. In contrast, unpaired rows of Sn atoms are visible in the SnS<sub>2</sub> region of Figure 3d. In this case, the Sn atoms of the SnS<sub>2</sub> vdW layer all lie in the same plane, as shown in Figure 1a.

The cross-sectional TEM image in Figure 3d shows the SnS<sub>2</sub> region in sufficient detail to resolve the inter-layer vdW gap. An overlay shows the expected crystallographic lattice.<sup>[27]</sup> Similarly, the SnS inter-layer vdW spacing can be seen in Figure 3c overlaid with the corresponding lattice.<sup>[28]</sup> For SnS<sub>2</sub>, we estimate a lattice parameter along the *c*-axis of  $5.9 \pm 0.5$  Å. This is determined over six unit cells on the TEM image and is close to that (5.90 Å) reported in the literature.<sup>[27]</sup> Similarly, for SnS we estimate a lattice parameter of  $11.5 \pm 0.5$  Å, close to that (11.2 Å) reported in previous studies of SnS.<sup>[28]</sup> The *c*-lattice parameter



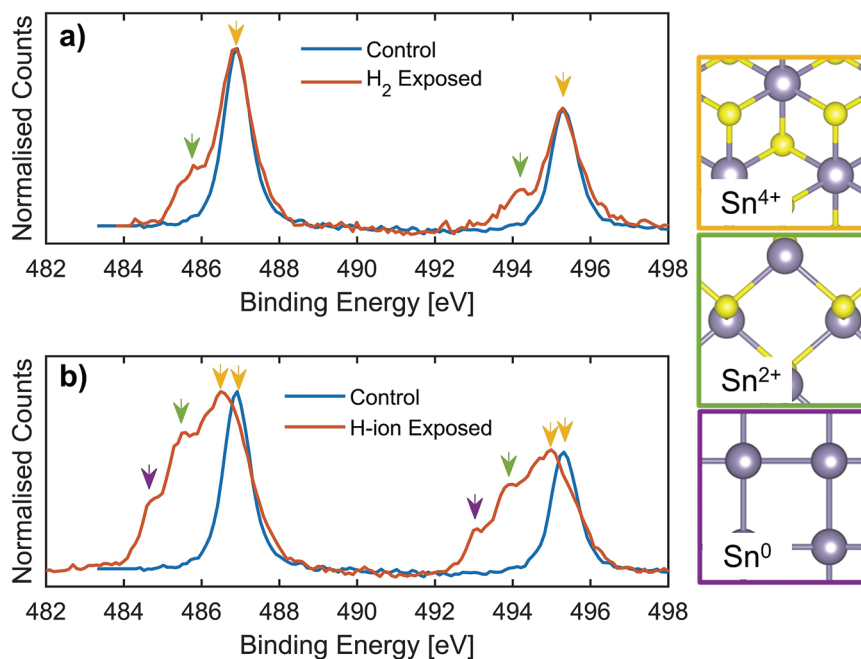


**Figure 2.** XPS Sn 3d core-level spectra for the control SnS<sub>2</sub> and SnS<sub>2</sub> exposed to a) H<sub>2</sub> for 7 h 40 min at  $7 \times 10^{-4}$  mbar and 150 °C, b) H-ions for 3 h 30 min with a beam energy of 12 eV and a total dose of  $6 \times 10^{-16}$  ions cm<sup>-2</sup>. Schematics show the crystal structures of SnS<sub>2</sub>, SnS and  $\beta$ -Sn with the corresponding Sn<sup>4+</sup>, Sn<sup>2+</sup>, and Sn<sup>0</sup> states marked on the XPS spectra with orange, green, and violet arrows, respectively.

is larger than for SnS<sub>2</sub> as the unit cell of SnS consists of two vdW layers.

Surface studies of the heterostructures by AFM show that the surface SnS layer retains a similar RMS roughness to the control sample at low doses ( $5 \times 10^{-4}$  mbar for 3.5 h at 150 °C). With

increasing hydrogen dose and/or exposure (>7 h), the roughness tends to increase (Figure S4, Supporting Information). Thus, under controlled hydrogen exposure conditions, it is possible to realize SnS<sub>2</sub>/SnS heterostructures with high-quality surfaces.

Under controlled exposure conditions, the heterostructure can retain well defined, uniform vibrational and optical properties, as probed by Raman and photoluminescence (PL) spectroscopy. **Figure 4a** compares the Raman spectra of three samples with and without exposure to H<sub>2</sub> and H-ions. For the control sample, the Raman peak at 314.5 cm<sup>-1</sup> is assigned to the A<sub>1g</sub> mode of SnS<sub>2</sub>. This compares favorably to previous reports of this mode between 314.3 and 318 cm<sup>-1</sup>.<sup>[23,36,37]</sup> The A<sub>1g</sub> mode can also be seen in the H<sub>2</sub> exposed sample, although with a lower intensity, together with four additional peaks centered at 95.1, 158.2, 185.1, and 224.1 cm<sup>-1</sup>. These are assigned to the A<sub>g</sub>, B<sub>3g</sub>, A<sub>g</sub>, and A<sub>g</sub> modes of SnS, respectively. They are in agreement with the modes expected for SnS layers for which the Raman peak positions are thickness dependent.<sup>[38,39]</sup> The linewidth of the SnS<sub>2</sub> A<sub>1g</sub> peak is unchanged by the exposure and the linewidths of the SnS components are in-line with those reported in the literature.<sup>[38,39]</sup> For the H-ion exposed sample, all the Raman peaks seen in the H<sub>2</sub> exposed sample are much weaker. In particular, the Raman peaks from SnS are centered at slightly different positions (96.2, 161.6, 189.1, and 221.1 cm<sup>-1</sup>), in-line with measurements of bulk SnS.<sup>[38,39]</sup> Also, an additional Raman feature is observed at 127.5 cm<sup>-1</sup>, which is assigned to the  $\Gamma_5$  mode of  $\beta$ -Sn.<sup>[40]</sup> Additionally, the possibility of forming either  $\alpha$ -Sn or stanene was considered, but none of the associated Raman peaks could be resolved.

Figure 4b shows the evolution of the Raman signal for a single SnS<sub>2</sub> film upon repeated exposures to H<sub>2</sub>. Here, the Raman spectra are normalized to the A<sub>1g</sub> peak of SnS<sub>2</sub>,

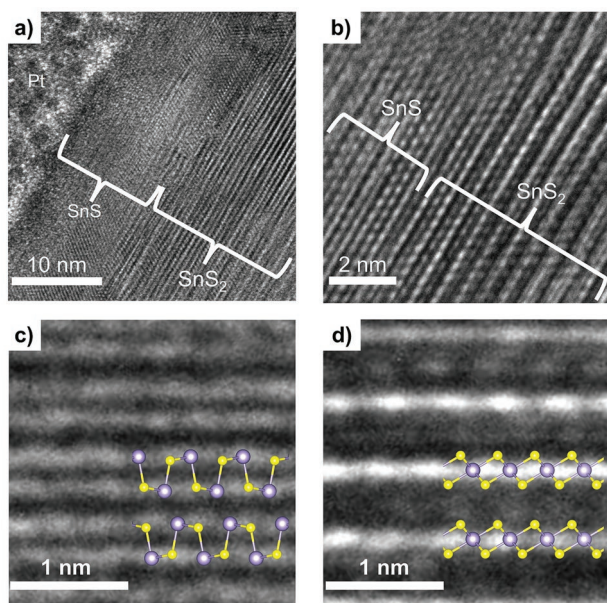


**Figure 3.** a) Cross-sectional TEM image of a H<sub>2</sub> exposed sample ( $5 \times 10^{-4}$  mbar, 150 °C for 7 h). b) Cross-sectional TEM images of a H<sub>2</sub> exposed sample showing the SnS-SnS<sub>2</sub> interface. c) Overlay of the expected SnS lattice with TEM data. d) Overlay of the expected SnS<sub>2</sub> lattice with TEM data.

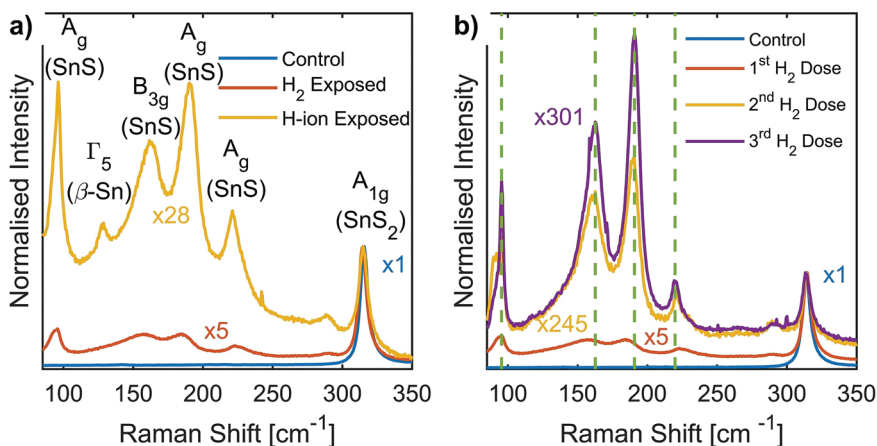


**Figure 4.** a) Raman spectra of SnS<sub>2</sub> samples (control and hydrogenated samples) at 300 K and  $\lambda = 632.8$  nm. b) Raman spectra of SnS<sub>2</sub> repeatedly exposed to H<sub>2</sub>. The green dashed lines indicate the positions of SnS peaks after the third dose.

revealing that with increasing exposure time, the Raman signal due to SnS become stronger relative to that of SnS<sub>2</sub>. The positions of the SnS peaks also shift with each exposure in-line with an increase of the SnS layer thickness.<sup>[38,39]</sup> Similar Raman experiments on the pristine and annealed samples confirm that none of the SnS related peaks are present before H<sub>2</sub> exposure.

We have imaged the Raman signal to probe the uniformity of the layers over large areas. The Raman studies reveal a correlation between the color contrast in the optical image

(Figure 5a) and the corresponding Raman maps of the flakes (Figure 5b,c). Each Raman map is obtained by plotting the ratio  $r$  of the Raman signal intensity ( $I$ ) due to SnS and SnS<sub>2</sub>, that is,  $r = I(\text{SnS})/I(\text{SnS}_2)$ , under laser excitation wavelengths of  $\lambda = 532.0$  nm (Figures 5b) and  $\lambda = 632.8$  nm (Figure 5c). It can be seen that the value of  $r$  is different for flakes of different color and/or for different laser wavelengths. The color and contrast in the optical image are determined by the interference of light reflected and transmitted at the different interfaces of the air/flake/substrate system. Thus, the color changes as the

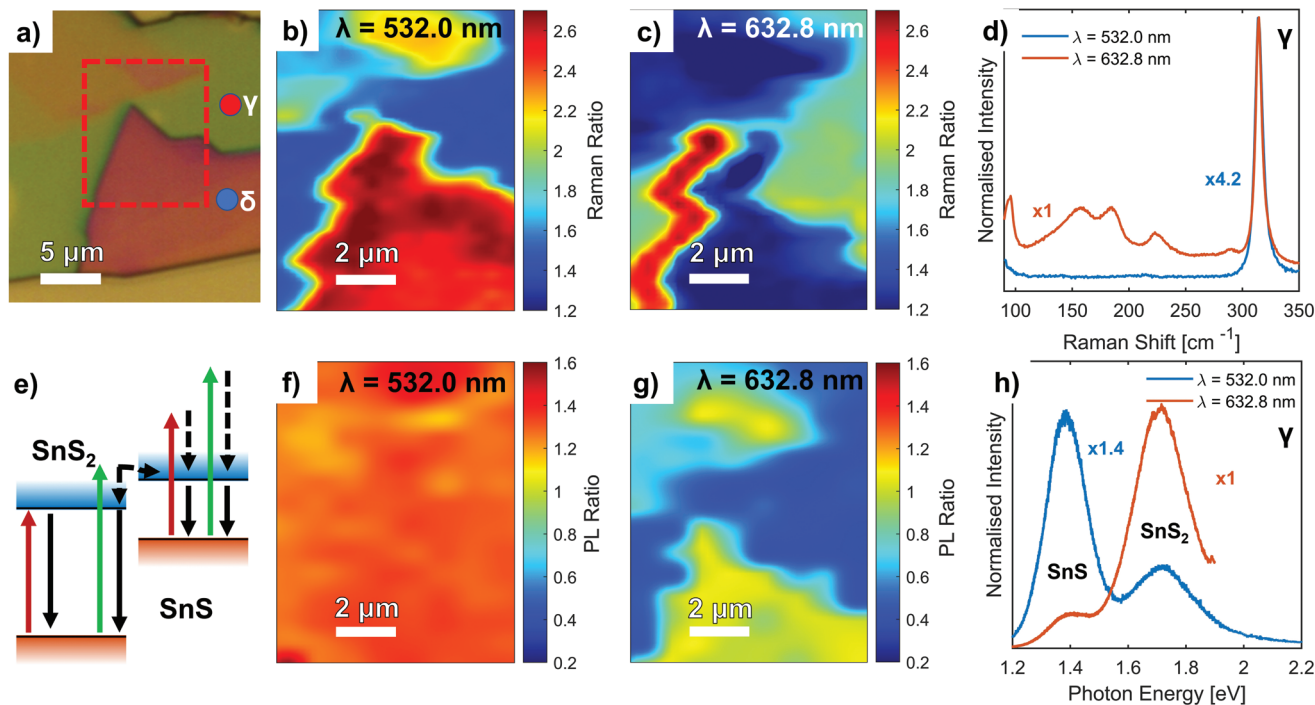


**Figure 5.** a) Optical image of the areas investigated in the Raman and PL maps as marked in red. Specific locations of the flake are marked as  $\gamma$  and  $\delta$ . b,c) Raman maps of the ratio of SnS to SnS<sub>2</sub> Raman signal for (b)  $\lambda = 532.0$  nm and (c)  $\lambda = 632.8$  nm. d) Raman spectra conducted on spot  $\gamma$  in part a). e) Type II band alignments of SnS<sub>2</sub> and SnS and optical transitions under laser excitation at 532.0 nm (green) and 632.8 nm (red). Dotted and continuous lines sketch relaxation and radiative recombination, respectively. The band alignment as determined experimentally in the literature.<sup>[34]</sup> f,g) PL maps of the ratio of SnS to SnS<sub>2</sub> PL signal with  $\lambda = 532$  nm (f) and  $\lambda = 632.8$  nm (g). h) PL spectra conducted on spot  $\gamma$  in (a).

thickness of the layers varies in the layer plane. For example, it is red (position  $\delta$ , Figure 5a) and green (position  $\gamma$ , Figure 5a), corresponding to layer thicknesses of 125 and 175 nm, respectively, as measured by AFM and shown in Figure S5, Supporting Information. As shown in the Raman map of Figure 5b and Raman spectrum of Figure 5d, for 532.0 nm, the thicker regions of the flake (position  $\gamma$ ) have a stronger contribution from SnS<sub>2</sub> than thinner regions (position  $\delta$ ). The reverse is observed for 632.8 nm (Figure 5c,d). This dependence and its correlation with the color of the flake in the optical image (Figure 5a) can be accounted for by a light interference effect in which constructive (destructive) interference of light leads to a corresponding enhanced (reduced) light absorption by the SnS<sub>2</sub> layer and hence larger (smaller) Raman signal. This interference effect can be mapped out to the AFM image of the layer thickness and ignoring interference effects from the superficial thin ( $\approx 10$  nm) SnS layer (Figure S5, Supporting Information). Thus, Raman imaging provides a means of assessing the formation of the SnS layer and its uniformity over a scale of several microns. On the red and green regions of the flake in the optical image, the variation in the Raman ratio ( $r$ ) is found to be <8% and <14%, respectively.

Both bulk SnS<sub>2</sub> and SnS crystals have an indirect band gap and their in-plane lattice constants, interlayer distances and interlayer binding energies tend to be weakly dependent on the layer thickness. SnS<sub>2</sub> has an indirect band gap energy of 2.25 eV and a direct band-gap energy of 2.38 eV,<sup>[41,42]</sup> whilst SnS has an indirect band gap energy of 1.07 eV and a direct band gap energy of  $\approx 1.4$  eV.<sup>[43]</sup> With these considerations, and with reference to the absorption spectrum of SnS<sub>2</sub>,<sup>[41]</sup> we now consider the optical properties of the flakes by examining their band edge recombination (Figure 5e) under different excitation wavelengths. Figure 5f,g show the PL maps for the flake in Figure 5a. The corresponding PL spectra are displayed in Figure 5h and are characterized by two bands centered at around 1.7 and 1.4 eV, whose relative weight changes with the excitation wavelength. The PL band centered at 1.7 eV is red-shifted relative to the absorption edge of SnS<sub>2</sub>, suggesting a dominant recombination of carriers from localized states. The PL band centered at 1.4 eV was previously reported in SnS and SnS-inclusions in SnS<sub>2</sub>.<sup>[29,44]</sup> The absence of a sizable optical anisotropy of the PL emission (Figure S6, Supporting Information), expected for SnS,<sup>[45,46]</sup> suggests that the PL emission at 1.4 eV in our structures arises from the recombination of carriers from localized states.<sup>[29]</sup> Thus, this PL band may not share the same optical characteristics of the band edge recombination.

The ratio of the integrated PL intensities,  $r = I(1.4 \text{ eV})/I(1.7 \text{ eV})$ , is  $\approx 1.2$  and is uniform in the layer plane (Figure 5f)). Thus, the emission from SnS tends to dominate the PL emission and is uniform, suggesting that the hydrogenation leads to a homogeneous conversion of the SnS<sub>2</sub> surface onto SnS. Furthermore, this indicates a preferential relaxation of photogenerated carriers from SnS<sub>2</sub> onto SnS. Increasing  $\lambda$  from 532.0 nm to 632.8 nm results in a stronger recombination signal from the 1.7 eV band relative to the 1.4 eV band (Figure 5h). The PL spectra under different excitation wavelengths can be understood in terms of different relaxation pathways for carriers and by referring to the schematic of Figure 5e. Since the SnS/SnS<sub>2</sub> heterostructure has a type II band alignment with a band offset

of 0.51 eV in the conduction band,<sup>[34]</sup> under resonant excitation ( $\lambda = 632.8$  nm) of the SnS<sub>2</sub> layer, electrons photogenerated in SnS<sub>2</sub> cannot relax onto SnS, leading to a larger signal from SnS<sub>2</sub> relative to SnS and corresponding decrease of  $r$  (Figure 5g). This result is supported by PL excitation (PLE) measurements over an extended energy range (Figure S7, Supporting Information) showing that the PL emission centered at 1.4 eV (attributed to SnS) tends to fall for excitation energies approaching the band gap energy of SnS<sub>2</sub>. Finally, the PL spectra show no evidence of an interlayer excitonic recombination. However, this is not unexpected due to the relatively thick SnS and SnS<sub>2</sub> layers.

### 3. Discussion

The results of the Raman, TEM, and XPS studies point clearly to a conversion of SnS<sub>2</sub> to SnS through exposure to H<sub>2</sub>. Furthermore, the cross-sectional TEM images reveal clearly how this conversion produces a heterostructure with a sharp transition from SnS<sub>2</sub> to SnS. Importantly, as with the exfoliation and stamping method frequently used in lab-scale manufacture of vdW heterostructures, the  $c$ -axes of both SnS<sub>2</sub> and SnS are coaxial and reveal continuous unbroken layers.

The uniformity of the heterostructure and its interface, as revealed by TEM, is further confirmed by Raman images. These show Raman signals from the heterostructure that are uniform over extended (micron) regions. Also, the Raman measurements demonstrate the possibility for controlling the formation and properties of the heterostructure via exposure time or repeated exposures, resulting in an increasing Raman intensity ratio  $I(\text{SnS})/I(\text{SnS}_2)$  and shift of the Raman modes due to SnS.

The further conversion of SnS to  $\beta$ -Sn was also considered using a H-ion beam and confirmed by XPS, EDX, and Raman data. The formation of extended plateau features observed in the optical (Figure 1) and SEM (Figure S2, Supporting Information) images is explained by the increased density of Sn in  $\beta$ -Sn (35.3 atoms nm<sup>-3</sup>) than in SnS (19.6 atoms nm<sup>-3</sup>) and SnS<sub>2</sub> (14.7 atoms nm<sup>-3</sup>), resulting in a contraction of the crystal as SnS is converted to  $\beta$ -Sn. This behavior is inline with previous reports of etching of SnS by hydrogen plasma.<sup>[47]</sup> A similar etching behavior is observed in our samples exposed to H<sub>2</sub> at temperatures greater than 250 °C.

We performed density functional theory calculations (computational details in Experimental Section) to examine the reaction energetics for the conversion of SnS<sub>2</sub> to SnS via H<sub>2</sub>. We summarize our results in **Table 1**. We find that the direct conversion of SnS<sub>2</sub> to SnS without H<sub>2</sub> (Reaction 1) is endothermic, that is, the reaction is not energetically favorable. However, in the presence of H<sub>2</sub>, the conversion (Reaction 2) becomes exothermic and energetically favorable, with the formation of H<sub>2</sub>S as a by-product. Further conversion of SnS to  $\beta$ -Sn, either with (Reaction 6) or without H<sub>2</sub> (Reaction 5), is endothermic. Similarly, the conversion of SnS<sub>2</sub> to  $\beta$ -Sn, either with (Reaction 4) or without H<sub>2</sub> (Reaction 3), is also endothermic. We note that the presence of H<sub>2</sub> makes the conversion of SnS<sub>2</sub> or SnS to  $\beta$ -Sn (Reactions 4 and 6) less endothermic, by 85.6 and 42.8 kJ mol<sup>-1</sup>, respectively. Thus, the DFT calculated reaction energies explain well our experimental observation on why H<sub>2</sub> treatment promotes the conversion of SnS<sub>2</sub> to SnS, but further conversion



**Table 1.** DFT predicted reaction energies ( $\Delta E$ , in  $\text{kJ mol}^{-1}$ ) of selected reactions. Positive  $\Delta E$  indicates the reaction is endothermic, and negative  $\Delta E$  indicates the reaction is exothermic. The symbol in the brackets denotes the phase of the reactants/products, “s” for solid and “g” for gas.

Index	Reaction	$\Delta E$ [ $\text{kJ mol}^{-1}$ ]
1	$\text{SnS}_2(\text{s}) \rightarrow \text{SnS}(\text{s}) + \text{S}(\text{s})$	+8.6
2	$\text{SnS}_2(\text{s}) + \text{H}_2(\text{g}) \rightarrow \text{SnS}(\text{s}) + \text{H}_2\text{S}(\text{g})$	-34.1
3	$\text{SnS}_2(\text{s}) \rightarrow \text{Sn}(\text{s}) + 2\text{S}(\text{s})$	+114.5
4	$\text{SnS}_2(\text{s}) + 2\text{H}_2(\text{g}) \rightarrow \text{Sn}(\text{s}) + 2\text{H}_2\text{S}(\text{g})$	+28.9
5	$\text{SnS}(\text{s}) \rightarrow \text{Sn}(\text{s}) + \text{S}(\text{s})$	+105.8
6	$\text{SnS}(\text{s}) + \text{H}_2(\text{g}) \rightarrow \text{Sn}(\text{s}) + \text{H}_2\text{S}(\text{g})$	+63.0

to  $\beta$ -Sn requires higher temperatures or longer exposure times. Conversion to  $\beta$ -Sn by H-ions is facilitated by the increased reactivity of the charged species and the additional 12 eV kinetic energy of the ions above the energies available to  $\text{H}_2$ .

The formation of a well-defined ordered interface between  $\text{SnS}_2$  and SnS (Figure 3) is an unexpected outcome. The thickness of the layer is controllable through repeated dosing with hydrogen (Figure 4b)). This observation points to a limited ability for hydrogen to penetrate into or react with  $\text{SnS}_2$  at a significant distance from the SnS/ $\text{SnS}_2$  interface. This might be explained by an enhanced reactivity near the interface or by differential diffusion rates of reactants/products in  $\text{SnS}_2$  and SnS.

We note that the chemical conversion of  $\text{SnS}_2$  to SnS could be facilitated by the presence of S-vacancies, a common defect in  $\text{SnS}_2$ ,<sup>[48]</sup> with a stronger binding energy to  $\text{H}_2$ , that is, the reaction may initiate from S-vacancies present on the  $\text{SnS}_2$  surface, propagate within the layer, followed by continued reaction into other layers. It is notable that these defects can be induced, for example via an electron beam, and that these defects introduce deep states within the band-gap.<sup>[44,49]</sup> For  $\text{SnS}_2$  exposed to H-ions, the conversion to  $\beta$ -Sn, as observed in our experiment, might be ascribed to the higher reactivity of H-ions. Note that  $\text{H}_2$  has a dissociation energy of  $432 \text{ kJ mol}^{-1}$ ,<sup>[50]</sup> and this may render Reactions 4 and 6 exothermic if  $\text{H}_2$  is replaced by protons as reactants.

In summary, DFT confirms that the conversion from  $\text{SnS}_2$  to SnS by  $\text{H}_2$  is energetically favorable. As shown by XPS and Raman studies, the further conversion of SnS to  $\beta$ -Sn is less favorable.

## 4. Conclusion

The ability of hydrogen to bond with sulfur was used to induce a controlled chemical conversion of  $\text{SnS}_2$  into semiconducting-SnS or  $\beta$ -Sn. These chemical conversions were successfully applied to form heterostructures with uniform layers, atomically flat interfaces and well-aligned crystallographic axes. The formation of an heterostructure by molecular hydrogen can be controlled via exposure time and temperature. Theoretical results support the experimental data and suggest a nucleation based growth mechanism as a reason for the uniformity of the layers. The significance of these results is twofold. First, they have relevance to post-growth

methods for the formation and patterning of  $\text{SnS}_2/\text{SnS}$  heterostructures. In contrast to previous methods that used argon plasma, large organic molecules, sulfurization, and magnetron sputtering,<sup>[51–54]</sup> the exposure of the layers to  $\text{H}_2$  stands out due to its simplicity and ability to produce a well defined interface and aligned *c*-axes. Thus, this proves promising for exploitation of  $\text{SnS}_2/\text{SnS}$  in heterojunction diodes,<sup>[51]</sup>  $\text{NO}_2$  detectors,<sup>[55]</sup> and other opto-electronic devices.<sup>[56]</sup> Second, these findings are relevant to the hydrogen technologies, where the strong interaction between  $\text{H}_2$  and  $\text{SnS}_2$  demonstrated here could provide a platform for sensing, purification, or generation technologies.

## 5. Experimental Section

**Materials—Growth and Post-Growth Hydrogenation:** Crystals of  $\text{SnS}_2$  were grown using the chemical vapor transport method in a 650 to 500 °C temperature gradient. An optical characterization of the as-grown crystals is given by Kudrynskiy et al.<sup>[29]</sup>

Flakes were exfoliated from bulk crystals to refresh their surfaces using adhesive tape. The exfoliated flakes were then stamped directly onto either Au/Si or  $\text{SiO}_2/\text{Si}$  substrates.

For those samples exposed to  $\text{H}_2$ , the substrates were loaded into a chamber which was then evacuated to pressures of less than  $\approx 10^{-5}$  mbar. Once under vacuum, the samples were heated with either a heating lamp or current heater. Whilst the pumps remained on,  $\text{H}_2$  was added to the chamber from a gas bottle with the pressure inside the chamber controlled via the  $\text{H}_2$  flow rate. This arrangement ensured that the hydrogen in the chamber was continually refreshed and any volatile products were evacuated. After the exposure time had elapsed, the hydrogen supply was shut-off and the samples allowed to cool under vacuum before removal from the chamber.

For samples exposed to H-ions, the samples were loaded into, pumped down, and heated using the same methods as for  $\text{H}_2$  exposed samples. The samples were grounded and exposed to a H-ion beam of fixed energy by a Kaufman ion source.<sup>[30]</sup> The beam produced contained a ratio of  $\text{H}^+/\text{H}_2^+$  of 0.0291.<sup>[57]</sup> After exposure the samples were allowed to cool under vacuum before removal from the chamber.

**Experimental Techniques:** Cross-sectional TEM was conducted on a sample of  $\text{SnS}_2$  exposed to  $\text{H}_2$  at  $7 \times 10^{-4}$  mbar at 150 °C for 7 h on a gold substrate. The sample was reinforced using electron and ion beam deposited platinum before milling in a Zeiss Crossbeam 550 (HR-CAT-SEM). TEM analysis was then conducted in a JEOL 2100F FEG-TEM equipped with an Oxford Instruments INCA EDX system.

XPS was conducted using a Kratos AXIS ULTRA with a monochromated Al  $K\alpha$  X-ray source (1486.6 eV) operated at 10 mA emission current and 12 kV anode potential (120 W). All XPS studies were conducted on samples stamped onto gold substrates to reduce charging and to provide calibration. Three locations were investigated on each sample with the beam encompassing a large distribution of flakes. The data was processed using CASA-XPS.

EDX spectra were taken using a JEOL 7000F FEG-SEM. All the samples investigated were on gold substrates and the data was analyzed using Oxford Instruments AZtec software.

The experimental setup for the micro-Raman and micro-PL spectroscopy studies at room temperature comprised a He-Ne laser (632.8 nm) and a frequency-doubled Nd:YVO4 laser (532.0 nm), an *x-y-z* motorized stage, and an optical confocal microscope system from Horiba Scientific equipped with a 0.5 m long monochromator with 1200 and 150  $\text{g mm}^{-1}$  gratings. The laser beam was focused to a diameter of  $\approx 1 \mu\text{m}$  using a 100 $\times$  objective. The signal was detected by a Si-charge-coupled device camera. Polarization-resolved PL measurements were conducted by using a linearly-polarized, frequency-doubled Nd:YVO4 laser (532.2 nm). A polarizer was placed in the laser optical path (parallel to the laser polarization direction) to better filter out spurious polarizations.

A half waveplate was used to rotate the laser polarization with respect to the sample. An  $x$ - $y$  motorized stage was used for precise positioning on the flake. The laser was focused via a 100 $\times$  objective (spot of  $\approx 1 \mu\text{m}$ ) and the signal was collected through the same objective, in a backscattering configuration. The signal polarization was then selected through a combination of a half waveplate and a polarizer. The waveplate was mounted on a motorized stage and rotated during the measurements. The signal was dispersed by using a 0.2 m long monochromator with a 150 grooves  $\text{mm}^{-1}$  grating, and detected by a  $\text{N}_2$ -cooled Si-charge-coupled device camera. PLE measurements were conducted by using a picosecond supercontinuum laser (by NKT Photonics). The emission wavelength was selected through a tunable filter based on acousto-optic tunable filter technology, resulting in monochromatic beam with  $\approx 8 \text{ nm}$  full width at half maximum. The laser wavelength was varied between 530 and 800 nm in steps of 10–20 nm. An  $x$ - $y$  motorized stage was used for precise positioning on the flake. The laser was focused via a 100 $\times$  objective (spot of  $\approx 1 \mu\text{m}$ ) and the signal was collected through the same objective, in a backscattering configuration. The signal was filtered out by a 850 nm longpass filter, was dispersed by using a 0.2 m long monochromator with a 150 grooves  $\text{mm}^{-1}$  grating, and detected by a  $\text{N}_2$ -cooled Si-charge-coupled device camera. The intensity was monitored on the summit of the peak at 1.4 eV. The optical studies were performed at low excitation power to avoid excessive heating.

AFM was conducted using an Asylum Research Cypher-S AFM system in both noncontact AC mode and contact mode. Lattice resolved images were imaged using the lateral deflection channel. All other images were resolved using the height channel. The data was processed using the Gwyddion software package.

**Theoretical Techniques:** All DFT calculations were performed using the CP2K code,<sup>[58]</sup> which employed a mixed Gaussian/plane-wave basis set. Double- $\zeta$  polarization quality Gaussian basis sets and a 400 Ry plane-wave cutoff were employed for the auxiliary grid,<sup>[59]</sup> in conjunction with Goedecker–Teter–Hutter pseudopotentials.<sup>[60]</sup> Total energy calculations and structural optimizations, including both atomic coordinates and cell parameters, were performed under periodic boundary conditions at the hybrid DFT level using the PBE0 exchange and correlation functional,<sup>[61]</sup> which had 25 Hartree–Fock exchange (HFx), with Grimme’s D3 van der Waals correction (PBE0+D3).<sup>[62]</sup> The HFx calculations were significantly accelerated by using the auxiliary density matrix method implemented in CP2K.<sup>[63]</sup> A convergence threshold of  $1.0 \times 10^{-6}$  Hartree was used for the self-consistent field cycle, and structural optimizations were considered to have converged when the maximum force on all atoms falls below  $4.5 \times 10^{-4}$  Hartree bohr $^{-1}$ . All DFT calculations were performed in the  $\Gamma$ -point approximation with sufficiently large supercells,  $3 \times 3 \times 2$  for  $\text{SnS}_2$  (54 atoms per cell) and  $1 \times 3 \times 3$  for SnS (72 atoms per cell).

## Supporting Information

Supporting Information is available from the Wiley Online Library or from the author.

## Acknowledgements

This work was supported by a studentship from the EPSRC funded Fuel Cell and Their Fuels CDT [grant number EP/L015749/1]; the European Union’s Horizon 2020 research and innovation programme Graphene Flagship Core 3; and the National Academy of Sciences of Ukraine. The authors acknowledge the use of the Sulis supercomputer through the HPC Midlands+ Consortium, and the ARCHER2 supercomputer through membership of the U.K.’s HPC Materials Chemistry Consortium, which are funded by EPSRC Grant Nos. EP/T022108/1 and EP/R029431/1, respectively. The authors thank the Nanoscale and Microscale Research Centre (nmRC) for providing access to instrumentation for XPS and TEM studies and to Michael Fay, Christopher Parmenter, and Craig Stoppiello for their technical assistance.

## Conflict of Interest

The authors declare no conflict of interest.

## Data Availability Statement

The data that support the findings of this study are available from the corresponding author upon reasonable request.

## Keywords

heterostructures, hydrogen-induced conversion, tin disulfide, tin sulfide, van der Waals

Received: April 29, 2022

Revised: June 22, 2022

Published online:

- [1] C. Lee, X. Wei, J. W. Kysar, J. Hone, *Science* **2008**, *321*, 385.
- [2] P. Miró, M. Audiffred, T. Heine, *Chem. Soc. Rev.* **2014**, *43*, 6537.
- [3] M. Orlita, C. Faugeras, P. Plochocka, P. Neugebauer, G. Martinez, D. K. Maude, A.-L. Barra, M. Sprinkle, C. Berger, W. A. de Heer, M. Potemski, *Phys. Rev. Lett.* **2008**, *101*, 267601.
- [4] G. G. Naumis, S. Barraza-Lopez, M. Oliva-Leyva, H. Terrones, *Rep. Prog. Phys.* **2017**, *80*, 096501.
- [5] G. R. Bhimanapati, Z. Lin, V. Meunier, Y. Jung, J. Cha, S. Das, D. Xiao, Y. Son, M. S. Strano, V. R. Cooper, L. Liang, S. G. Louie, E. Ringe, W. Zhou, S. S. Kim, R. R. Naik, B. G. Sumpter, H. Terrones, F. Xia, Y. Wang, J. Zhu, D. Akinwande, N. Alem, J. A. Schuller, R. E. Schaak, M. Terrones, J. A. Robinson, *ACS Nano* **2015**, *9*, 11509.
- [6] A. Gupta, T. Sakhivel, S. Seal, *Prog. Mater. Sci.* **2015**, *73*, 44.
- [7] D. Cheng, H. Y. Yang, *Adv. Mater.* **2018**, *30*, 1800865.
- [8] J. W. Jang, C. E. Lee, C. I. Oh, C. J. Lee, *J. Appl. Phys.* **2005**, *98*, 074316.
- [9] S. Ryu, M. Y. Han, J. Maultzsch, T. F. Heinz, P. Kim, M. L. Steigerwald, L. E. Brus, *Nano Lett.* **2008**, *8*, 4597.
- [10] E. Grånäs, T. Gerber, U. A. Schröder, K. Schulte, J. N. Andersen, T. Michely, J. Knudsen, *Surf. Sci.* **2016**, *651*, 57.
- [11] R. Yang, L. Zhang, Y. Wang, Z. Shi, D. Shi, H. Gao, E. Wang, G. Zhang, *Adv. Mater.* **2010**, *22*, 4014.
- [12] S. Hu, M. Lozada-Hidalgo, F. Wang, A. Mishchenko, F. Schedin, R. R. Nair, E. Hill, D. Boukhvalov, M. Katsnelson, R. A. Dryfe, I. V. Grigorieva, H. A. Wu, A. K. Geim, *Nature* **2014**, *516*, 227.
- [13] J. Felton, E. Blundo, S. Ling, J. Glover, Z. R. Kudrynskiy, O. Makarovskiy, Z. D. Kovalyuk, E. Besley, G. Walker, A. Polimieni, A. Patané, *Molecules* **2020**, *25*, 2526.
- [14] D. Tedeschi, E. Blundo, M. Felici, G. Pettinari, B. Liu, T. Yildirim, E. Petroni, C. Zhang, Y. Zhu, S. Sennato, Y. Lu, A. Polimieni, *Adv. Mater.* **2019**, *31*, 1903795.
- [15] P. Kumar, S. Singh, S. Hashmi, K.-H. Kim, *Nano Energy* **2021**, *105989*.
- [16] P. Ganguly, M. Harb, Z. Cao, L. Cavallo, A. Breen, S. Dervin, D. D. Dionysiou, S. C. Pillai, *ACS Energy Lett.* **2019**, *4*, 1687.
- [17] T. K. N. Pham, J. J. Brown, *Chem. Sel.* **2020**, *5*, 24.
- [18] M. Lozada-Hidalgo, S. Hu, O. Marshall, A. Mishchenko, A. Grigorenko, R. Dryfe, B. Radha, I. Grigorieva, A. Geim, *Science* **2016**, *351*, 68.
- [19] IEA, *Global Hydrogen Review 2021* **2021**, <https://www.iea.org/reports/global-hydrogen-review-2021>.
- [20] S. J. Pearton, J. W. Corbett, M. Stavola, *Hydrogen in Crystalline Semiconductors*, Vol. 16, Springer, Berlin, Heidelberg **2013**.



- [21] J. M. Skelton, L. A. Burton, F. Oba, A. Walsh, *J. Phys. Chem. C* **2017**, *121*, 6446.
- [22] J. M. Gonzalez, I. I. Oleynik, *Phys. Rev. B* **2016**, *94*, 125443.
- [23] T. Sriv, K. Kim, H. Cheong, *Sci. Rep.* **2018**, *8*, 10194.
- [24] S. R. Damkale, S. S. Arbut, G. G. Umarji, R. P. Panmand, S. K. Khore, R. S. Sonawane, S. B. Rane, B. B. Kale, *Sustainable Energy Fuels* **2019**, *3*, 3406.
- [25] B. Sainbileg, Y.-R. Lai, L.-C. Chen, M. Hayashi, *Phys. Chem. Chem. Phys.* **2019**, *21*, 26292.
- [26] S. A. Patil, H. T. Bui, S. Hussain, I. Rabani, Y. Seo, J. Jung, N. K. Shrestha, H. Kim, H. Im, *Dalton Trans.* **2021**, *50*, 12723.
- [27] O. Madelung, U. Rössler, M. Schulz, *Landolt-Börnstein - Group III Condens. Matter* **1998**, *41C*, 1.
- [28] T. Chattopadhyay, J. Pannetier, H. Von Schnering, *J. Phys. Chem. Solids* **1986**, *47*, 879.
- [29] Z. R. Kudrynskiy, X. Wang, J. Sutcliffe, M. A. Bhuiyan, Y. Fu, Z. Yang, O. Makarovskiy, L. Eaves, A. Solomon, V. T. Maslyuk, Z. D. Kovalyuk, L. Zhang, A. Patané, *Adv. Funct. Mater.* **2020**, *30*, 1908092.
- [30] H. R. Kaufman, *An Ion Rocket with an Electron-Bombardment Ion Source*, National Aeronautics and Space Administration, Washington, D. C **1961**.
- [31] B. Li, T. Xing, M. Zhong, L. Huang, N. Lei, J. Zhang, J. Li, Z. Wei, *Nat. Commun.* **2017**, *8*, 1958.
- [32] J. Chastain, R. C. King Jr, *Handbook of X-Ray Photoelectron Spectroscopy*, Perkin-Elmer Corporation, Waltham, MA **1992**.
- [33] V. R. M. Reddy, S. Gedi, C. Park, R. Miles, K. T. R. Reddy, *Curr. Appl. Phys.* **2015**, *15*, 588.
- [34] T. J. Whittles, L. A. Burton, J. M. Skelton, A. Walsh, T. D. Veal, V. R. Dhanak, *Chem. Mater.* **2016**, *28*, 3718.
- [35] J. F. Moulder, W. F. Stickle, P. E. Sobol, K. D. Bomben, *Handbook of X-Ray Photoelectron Spectroscopy*, Perkin-Elmer Corporation, Eden Prairie, MN **1992**.
- [36] D. Mead, J. Irwin, *Solid State Commun.* **1976**, *20*, 885.
- [37] Y. Ding, W. Zheng, X. Lu, Y. Liang, Y. Zhu, M. Jin, F. Huang, *J. Phys. Chem. Lett.* **2020**, *11*, 10094.
- [38] J. Xia, X.-Z. Li, X. Huang, N. Mao, D.-D. Zhu, L. Wang, H. Xu, X.-M. Meng, *Nanoscale* **2016**, *8*, 2063.
- [39] M. Li, Y. Wu, T. Li, Y. Chen, H. Ding, Y. Lin, N. Pan, X. Wang, *RSC Adv.* **2017**, *7*, 48759.
- [40] E. P. y Blancá, A. Svane, N. Christensen, C. Rodriguez, O. Cappannini, M. Moreno, *Phys. Rev. B* **1993**, *48*, 15712.
- [41] Z. Yang, X. Wang, J. Felton, Z. Kudrynskiy, M. Gen, T. Nomura, X. Wang, L. Eaves, Z. D. Kovalyuk, Y. Kohama, L. Zhang, A. Patané, *Phys. Rev. B* **2021**, *104*, 085206.
- [42] L. A. Burton, T. J. Whittles, D. Hesp, W. M. Linhart, J. M. Skelton, B. Hou, R. F. Webster, G. O'Dowd, C. Reece, D. Cherns, D. J. Fermin, T. D. Veal, V. R. Dhanak, A. Walsh, *J. Mater. Chem. A* **2016**, *4*, 1312.
- [43] J. Vidal, S. Lany, M. d'Avezac, A. Zunger, A. Zakutayev, J. Francis, J. Tate, *Appl. Phys. Lett.* **2012**, *100*, 032104.
- [44] P. Sutter, H.-P. Komsa, A. Krashennnikov, Y. Huang, E. Sutter, *Appl. Phys. Lett.* **2017**, *111*, 262102.
- [45] C. Chen, X. Chen, Y. Shao, B. Deng, Q. Guo, C. Ma, F. Xia, *ACS Photonics* **2018**, *5*, 3814.
- [46] S. Lin, A. Carvalho, S. Yan, R. Li, S. Kim, A. Rodin, L. Carvalho, E. M. Chan, X. Wang, A. H. Castro Neto, J. Yao, *Nat. Commun.* **2018**, *9*, 1455.
- [47] Z. Xiao, F.-Y. Ran, M. Liao, H. Hiramatsu, K. Ide, H. Hosono, T. Kamiya, *Phys. Chem. Chem. Phys.* **2018**, *20*, 20952.
- [48] Y. Gong, H. Yuan, C.-L. Wu, P. Tang, S.-Z. Yang, A. Yang, G. Li, B. Liu, J. van de Groep, M. L. Brongersma, M. F. Chisholm, S.-C. Zhang, W. Zhou, Y. Cui, *Nat. Nanotechnol.* **2018**, *13*, 294.
- [49] Y. Kumagai, L. A. Burton, A. Walsh, F. Oba, *Phys. Rev. Appl.* **2016**, *6*, 014009.
- [50] G. Herzberg, A. Monfils, *J. Mol. Spectrosc.* **1961**, *5*, 482.
- [51] J. H. Kim, S. J. Yun, H. S. Lee, J. Zhao, H. Bouzid, Y. H. Lee, *Sci. Rep.* **2018**, *8*, 10284.
- [52] S. Gedi, V. R. M. Reddy, B. Pejjai, C.-W. Jeon, C. Park, K. T. R. Reddy, *Appl. Surf. Sci.* **2016**, *372*, 116.
- [53] A. Degrauw, R. Armstrong, A. A. Rahman, J. Ogle, L. Whittaker-Brooks, *Mater. Res. Express* **2017**, *4*, 094002.
- [54] J. Kim, J. Kim, S. Yoon, J.-y. Kang, C.-W. Jeon, W. Jo, *J. Phys. Chem. C* **2018**, *122*, 3523.
- [55] Q. Sun, J. Wang, J. Hao, S. Zheng, P. Wan, T. Wang, H. Fang, Y. Wang, *Nanoscale* **2019**, *11*, 13741.
- [56] M. Li, Y. Zhu, T. Li, Y. Lin, H. Cai, S. Li, H. Ding, N. Pan, X. Wang, *Inorg. Chem. Front.* **2018**, *5*, 1828.
- [57] N. Bauer, J. Beach, *J. Chem. Phys.* **1947**, *15*, 150.
- [58] J. Hutter, M. Iannuzzi, F. Schiffmann, J. VandeVondele, *Wiley Interdiscip. Rev.: Comput. Mol. Sci.* **2014**, *4*, 15.
- [59] J. VandeVondele, J. Hutter, *J. Chem. Phys.* **2007**, *127*, 114105.
- [60] M. Krack, *Theor. Chem. Acc.* **2005**, *114*, 145.
- [61] M. Ernzerhof, G. E. Scuseria, *J. Chem. Phys.* **1999**, *110*, 5029.
- [62] S. Grimme, J. Antony, S. Ehrlich, H. Krieg, *J. Chem. Phys.* **2010**, *132*, 154104.
- [63] M. Guidon, J. Hutter, J. VandeVondele, *J. Chem. Theory Comput.* **2010**, *6*, 2348.